SPACEDUST-Laser/RF: Time of Flight Methods for Space Situational Awareness

William Ediger[a], Yue Ma[b], Matthew Driedger[c], Alex Gmerek[d], Renmar Khim Palma[a], Paul Harrison[c], Michael Berezin[c], Philip Ferguson[a], John Spray[e], Alex Ellery[d], James Kennedy[b]

[a]University of Manitoba; [b]C-CORE; [c]Magellan Aerospace; [d]Carleton University; [e]HIT Dynamics

ABSTRACT

Space and ground based space situational awareness (SSA) platforms are critical for identifying and tracking RSOs. However, as the RSO population continues to grow, additional SSA platforms and methods for detecting RSOs will become necessary. This paper presents current efforts by Magellan Aerospace and its collaborators at the University of Manitoba, C-CORE, Carleton University, and HIT Dynamics to develop time-of-flight methods for detecting RSOs in low Earth orbit (LEO). With funding provided by Canada's Department of National Defence, Magellan and its partners are developing a optical/laser RSO detection prototype and investigating SAR-based RSO detection methods as part of the SPACEDUST (Special Processes and Advanced Computing Environment for Detection, Unambiguity, Surveying, and Tracking) project.

1. INTRODUCTION

As the number of spacecraft in orbit around the Earth continues to increase, so does the population of derelict satellites and other space debris. Collectively these objects, alongside active spacecraft and natural objects, are known as Resident Space Objects (RSOs). Space-based Space Situational Awareness (SSA) platforms are becoming more critical to identify and track RSOs to prevent on-orbit collisions and the further propagation of RSOs. However, the cost and development-time necessary for dedicated SSA missions mean that not enough SSA platforms are available. Those dedicated space-based SSA observatories that are available, such as Sapphire and NEOSSAT, are limited in number and are focused on tracking full-size satellites. Additionally, most SSA satellites rely on angle-based optical tracking methods, which have difficulties in establishing a full orbital solution for a detected object on their own, and would greatly benefit from time-of-flight information to provide complete orbital solutions. This paper describes current efforts by Magellan Aerospace, the University of Manitoba, C-CORE, Carleton University, and HIT Dynamics Ltd to develop time-of-flight based sensors and techniques that can be used to contribute to orbital SSA capabilities as a part of our ongoing SPACEDUST (Special Processes and Advanced Computing Environment for Detection, Unambiguity, Surveying, and Tracking) project. Specifically, this paper presents the preliminary design and testing of an optical/laser ranging sensor and techniques for extracting RSO-range data from Synthetic Aperture Radar (SAR) images.

1.1 Laser and LiDAR Technologies

Terrestrial observatories using laser rangefinders have been able to successfully detect RSOs without retroreflectors up to distances of 3000 km [1]. However, terrestrial ranging systems are limited to operating during only a few select hours of the day, as daylight observations of RSOs are limited by the contrast of RSOs against the sky [1]. This limitation may be addressed by implementing laser ranging solutions on space-based platforms. Additionally, space-based laser ranging platforms have the potential to provide host spacecraft with independent close proximity warning capabilities.

Three broad categories of laser pointing solutions were identified as possible candidates for time-of-flight ranging devices. These categories were outlined by [2] as common acquisition, tracking, and pointing solutions for free-space optical communications systems. Reference [2] discusses the strengths and weaknesses of gimbal, mirror, and hybrid pointing systems when applied to optical communications systems. However, these findings can also be applicable to near-space time-of-flight object tracking devices.

Gimbal-based systems consist of a sensor, such as a laser rangefinder, mounted to a mechanical gimbal. The primary advantage of these systems lies in their extensive range of motion, capable of covering a wide field of view [2].

However, due to their relatively large angular step-sizes, considerable mass, and susceptibility to wear, these systems present key limitations when applied to space-based missions.

Mirror-based systems utilize a reliable high speed mirror to redirect a laser beam towards a desired object. Three conventional options for such systems are fast-steering mirrors, piezoelectric systems, and micro-electromechanical systems (MEMS) [2]. Fast-steering mirrors (FSM) can achieve highly reliable measurements employing a very small angular step size through a large range of motion [2]. The voice-coil technology used for most FSMs means that these systems are lightweight and wear-resistant. Piezoelectric devices have extremely precise control, at the cost of limited range of motion and more complex control algorithms [2]. MEMS mirrors can provide fine control of a beam of light, but typically have much smaller mirror sizes compared to FSMs. Mirror size can limit the amount of light returned to a receiver, a concern for performing time-of-flight range measurements.

The aforementioned systems may be merged by mounting a mirror system on to a mechanical gimbal, thereby attaining an extended range of motion compared to a standalone mirror system, along with a higher pointing resolution than can be achieved solely through a gimbal mechanism [2]. While these systems improve performance, it is important to note that the aforementioned limitations of space-based gimbal systems persist.

Flash LiDAR is a unique type of system that does not require a pointing solution; instead range data is captured across a field of view in a single shot. These devices are desirable for space-based applications due to their wide field of views and lack of wear from moving components [3]. Flash LiDAR is limited in range compared to single-point rangefinders, for instance the unit described by [4] has a maximum detection range of 1.1 km. In contrast, single-point laser rangefinders (LRFs) can accurately range targets at distances greater than 5 km [5].

1.2 SAR Based RSO Detection

SAR is primarily used for Earth observation and monitoring by transmitting radio waves to the ground, receiving reflected signals, and processing signals to form SAR imagery. While intended for Earth observation, these reflected signals also contain reflections from RSOs orbiting between the SAR and Earth. Algorithms can be developed and applied on these raw, unprocessed received signals to extract RSO data, without affecting the SAR's primary Earth observation mission. Since there are numerous SAR satellites operating in orbit, using these platforms for RSO detection could greatly increase the probability of RSO detection and improve SSA capacity.

For instance, a case documented by the German Aerospace Center (DLR) involved the International Space Station (ISS) passing across the field-of-view of TerraSAR-X, Germany's remote sensing satellite [6]. The ISS was at a distance of approximately 195 km, travelling at a relative speed of 34,540 km/h [6]. Despite the encounter lasting only three seconds, this brief moment was long enough for TerraSAR-X to acquire a detailed image of the ISS. Fig. 1 shows a snapshot of the ISS image with a resolution of 1 m. It can be observed that, unlike optical imagery, the microwave signals transmitted by the radar are reflected back intensely by edges and corners. The German Aerospace Center stated that this orbital configuration could provide the opportunity for similar images between 10 and 11 times each month [6].
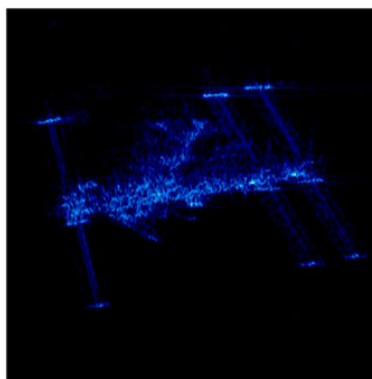

Fig. 1: Radar snapshot of the ISS [6].

Section 2 presents the preliminary design and testing of the SPACEDUST optical/laser tracking system (OLTS) while Section 3 presents the development and testing of our SAR-based RSO ranging methods. We conclude the paper in

Section 4.

2. OPTICAL/LASER PROTOTYPE

The OLTS is being designed as a self-contained SSA payload for integration into future satellites without compromising their primary missions. This section presents the preliminary engineering design for the OLTS, including calibration results, and outlines upcoming laboratory and field tests. Initial tests focus on validating the OLTS's performance during fixed target detection. We have designed the prototype with a future functional test in mind, involving the system tracking and ranging a high speed target. High speeds will be achieved by dropping a metallic cylinder (15 cm diameter, 90 cm length with a conical end) from a helicopter at altitudes of 500-1000 m. The system, hovering 100 m in the air on a drone, must track the falling target from a horizontal distance of 90 m. Previous field tests suggest that the target's relative angular rate, as perceived by the prototype, is expected to exceed 44 deg/s. This upcoming final test aims to demonstrate the prototype's ability to track and range targets travelling at high angular speeds, typical of orbit conjunction events between LEO satellites.

To meet the performance required for this final test, the system must be capable of visually identifying moving targets, using the visual information of identified targets to point the beam of a LRF to hit the target, and receiving the return beam to the LRF receiver to determine the range of the target. Target range and pointing angles must be recorded to determine the location of the target relative in three-dimensions relative to the system.

The system comprises a LRF, a FSM to direct the LRF beam, and a controller to facilitate commands to the devices. Additionally, the prototype incorporates a machine-learning-capable optical cueing camera to function as a proxy for visual RSO detection mechanisms, such as those outlined in [7]. Combined, this sensor is intended to provide users with relative RSO angle and range data that can be used to reconstruct an object's orbit. Based on our preliminary analysis, we expect this sensor to have a detection range sufficient to supply SSA data during conjunction events and to provide proximity-warning capabilities to a host spacecraft.

The maximum range of an LRF can be impacted by a target's albedo, limiting the amount of light capable of returning to the receiver of an LRF. To better understand the maximum range at which an LRF can detect RSOs on-orbit, we have developed a bench-top laser material reflectance test apparatus, described in detail in Section 2.5.

2.1 Operations

The OLTS uses a computer vision-enabled cueing camera to detect target objects. The centroid of a detected target is relayed to the prototype's main computer, which converts centroid data to pitch and yaw angles. These angles are used to direct the laser rangefinder's beam. Refer to Fig. 2 for a system block diagram for the system outlined above.

Targets travelling at very high relative speeds may drift outside of the LRF beam directed by the commanded pointing angle before a measurement is taken. Therefore, an optional scanning pattern was implemented to increase coverage of the LRF beam to capture targets that may drift outside the detected target area before a measurement could be made. The scanning pattern begins centered on the detected target centroid, followed by a series of concentric circles of increasing radii to provide equal coverage of the beam to account for any direction of motion. The average amount of time to complete a full round of camera object detection and FSM pointing was measured by calculating the average system framerate. We noted that the average system measurement speed was between 14.5 and 15.5 Hz when using a scanning pattern with a single circle of diameter less than 1 degree. The falling target that we will be using during the previously mentioned high speed test campaign is expected to travel approximately 3 degrees between measurements, falling outside the 1 deg wide scanning pattern used during measurement. Therefore this measurement speed was deemed insufficient for tracking a target travelling at angular speeds of 44 deg/s as required for the final functional tests. To ensure that the OLTS is able to reliably measure the high speed target for its full descent, we are examining several future improvements to the prototype as described in Section 2.6.
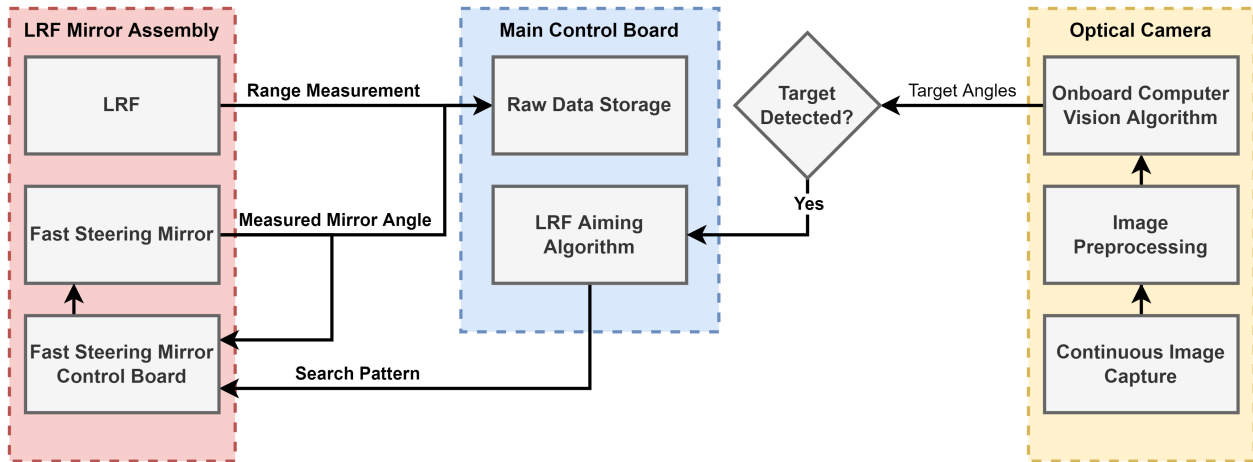
Fig. 2: OLTS Block Diagram.

2.2 Subsystems

The OLTS consists of a main control board interfacing with a fast-steering mirror (FSM), laser rangefinder (LRF), and optical cueing camera. All of these components are rigidly mounted to a structure that has been designed to attach to a DJI M300 drone for the future final functional test. An annotated image of the OLTS attached to the DJI M300 drone can be seen in Fig. 3.
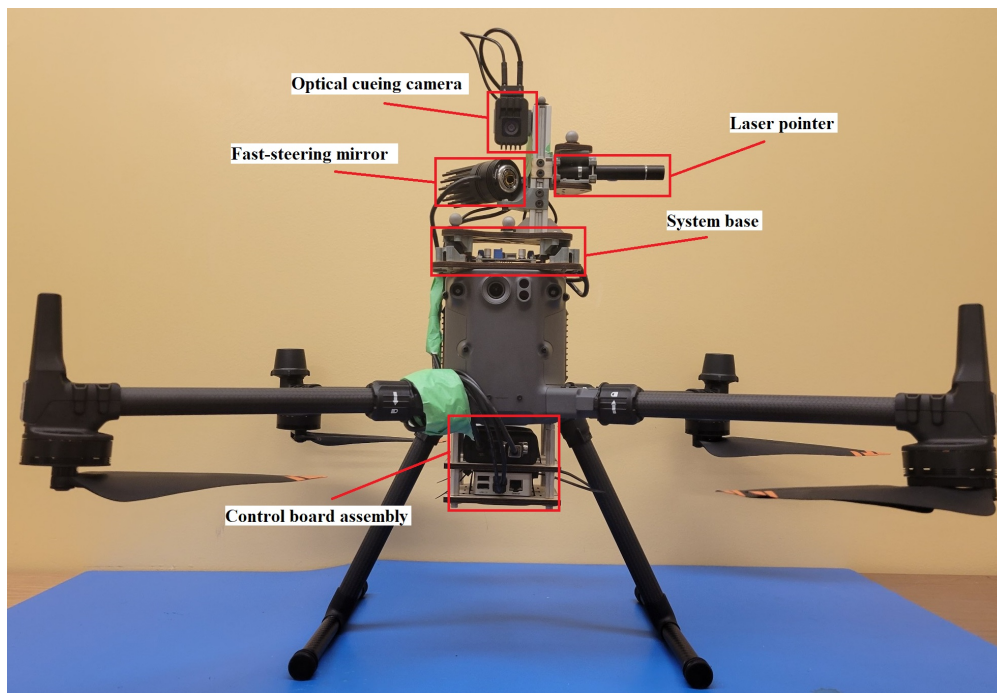

Fig. 3: Front view of the assembly, mounted on the M300 drone.

Control Board

We chose the Raspberry Pi 4 Model B as the main control board for the OLTS. This model is a compact single-board computer capable of running the operations of the OLTS. Notably, the Raspberry Pi 4 is features 4 USB-A ports that can accommodate the optical cueing camera, the FSM controller, and the LRF.

Laser Rangefinder

We chose the Jenoptik DLEM 20 due to its low weight, compactness, and low power consumption, suitable for use on small platforms such as micro-satellites or aerial drones. Due to the mass and size limitations of the DJI M300 drone the DLEM 20 was determined to be the most suitable LRF for preliminary ground and drone-based development, however the DLEM 20 may be replaced with a longer range LRF in the future.

Optical Cueing Camera

We selected the Luxonis OAK-1W computer vision camera for the prototype's cueing camera, due to onboard image processing capability, wide field of view, and high frame rate. For preliminary fixed and slow-moving target testing, we trained the cueing camera using the YOLOv5s network [8] to detect a 7.62 cm cube. The YOLOv5s neural network was selected as it is one of the fastest and least computationally expensive YOLO implementations available for the OAK-1W camera.

The Luxonis OAK-1W comes pre-trained to detect common objects. We retrained the YOLOv5s neural network to detect a target cube by using 1100 training images, taken at varying distances and lighting conditions within an office environment. The network was trained for 1000 epochs with batch sizes of 32. A further 107 images were used for validation and 55 images were used for testing. The precision-recall curve for the resulting trained network is shown in Fig. 4.
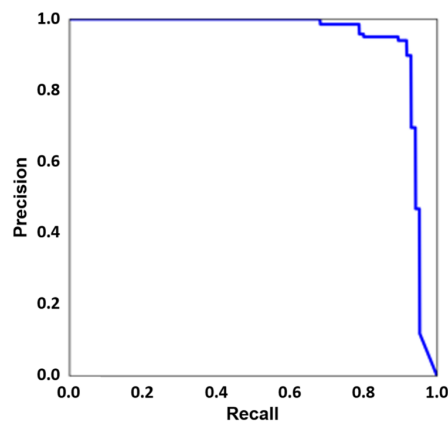

Fig. 4: Precision-recall curve for the cueing camera's YOLOv5s network, when retrained to detect the target cube.

This curve presents the relationship between the neural network's precision and recall rates for various detection thresholds between 0 and 1. These thresholds represent the minimum confidence in a detection required for a neural network to consider a proposed detection to be valid. Precision describes how frequently the neural network correctly identifies an object as the desired target and is defined as

$$Precision = \frac{T_P}{T_P + F_P} \tag{1}$$

where T_P is the number of true positive object detections and T_F is the number of false positive detections. Recall describes how frequently the neural network fails to detect a target and is defined as

$$Recall = \frac{T_P}{T_P + F_N} \tag{2}$$

where F_N is the number of false negatives. An ideal precision-recall curve would have a constant precision of unity for all recall values and a mean average precision (mAP) of 1. However, in real implementations a neural network will detect more false positives, experience fewer false negatives, and have a lower mAP as the detection threshold is decreased. The precision-recall curve for our retrained YOLOv5s neural network is acceptably close to an ideal curve, with a precision of approximately 0.9 for a recall of 0.9 and a mAP of 0.937. We were able to achieve this level of performance due to the relative simplicity of our target, the contrast between the target and its surroundings, and a lack of other objects that could be confused with the target in the verification image dataset. As discussed below, the neural

network experienced a greater number of false negatives during testing. However, the neural network's performance remained sufficient to develop the OLTS.

Fast-Steering Mirror

We chose the Optotune MR-15-30 as the FSM primarily for it's lightweight, compact size making this option suitable for a small mobile platform. The MR-15-30 has been implemented in other fine-pointing applications such as medical devices, optical communication systems, and automotive control systems [9]. The Optotune MR-15-30 features 2-axis tilt, allowing us to aim a beam in two dimensions. The maximum optical deflection angle of 50 degrees in both axes provides a FOV almost large enough to cover the entire optical cueing camera FOV.

Prototype Structure

We designed the prototype to be capable of operating attached and detached from a DJI M300 drone for testing purposes. The mirror and laser are attached rigidly to an extruded aluminum T-slot beam, aligned such that the laser beam hits the center of the FSM at approximately 45 degrees in the horizontal axis. The system attached to the DJI M300 drone can be seen in Fig. 3. The system is designed so the entire camera-mirror-laser assembly may be tilted at the base of the T-slot aluminum extrusion to adjust the angle of the entire system relative to the ground/base of the drone.

The sensor assembly is mounted on a custom damping plate to stabilize the camera by mitigating the effects of drone micro-vibrations during flight. The custom damping plate is based on the upward gimbal connector sold by DJI for the M300 [10]. We have yet to establish the effects of the damping plate on system performance during drone flight. The controller board assembly securely holds the main controller and FSM control board.

Prototype Power

The system was designed to operate independent of a wall power source, relying solely on the DJI M300 for power. All systems can be adequately powered by the drone equipped with backup batteries for a period exceeding 40 minutes. Based on experience with previous drop tests, a single test will take less than 20 minutes. As such, the power provided by the DJI M300 was determined to be adequate for the planned drop tests.

The USB-C and OSDK power ports of the DJI M300 are used to power the entire assembly. The main controller is powered through the 5V USB-C supply, whereas the FSM control board is powered via the 24 V OSDK port. Because of peripheral power limitations with the main controller the optical cueing camera is powered via a voltage regulator connected to the DJI M300's 24 V OSDK power port, while a data line is connected to the main controller. Fig. 5 illustrates the power and data distribution diagram for the system.
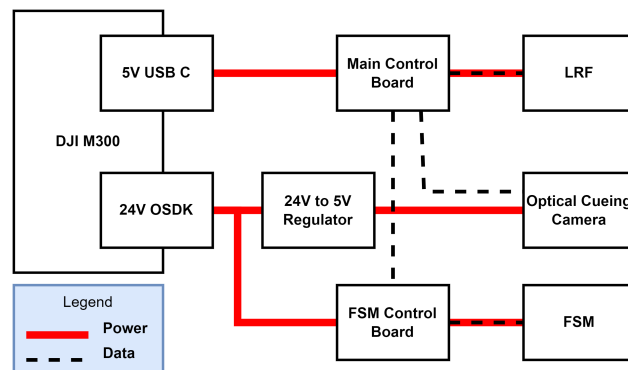

Fig. 5: Power and data distribution diagram.

2.3 Calibration

Calibration procedures were performed using a laser pointer to account for errors caused by assembly misalignment and possible camera image distortion. Data was gathered by affixing the target to a contrasting wall and performing two angular measurements taken with the FSM. The OLTS took an image with the target in frame, then based on the detected target pixel coordinates moved the FSM to where the OLTS expected the target to be and recorded the horizontal and vertical pointing angles provided by the FSM. A second angle measurement was taken by putting the FSM into a manual control mode, allowing an operator to jog the FSM until the laser hit the center of the target, once

hit the horizontal and vertical pointing angles were recorded. These two mirror pointing angle measurements were compared to calculate both horizontal and vertical errors for each target location. The above process was repeated for twenty eight points throughout the system field of view. Calibration data was processed to determine polynomial coefficients to fit a multi-variable polynomial to the measured error as a function of camera detected coordinates. The following equation was used to determine the polynomial fit for the horizontal (x) axis, the same form was used to find a polynomial fit in the vertical (y) axis.

$$\Delta X = BA \tag{3}$$

$$\begin{bmatrix} \Delta x_1 \\ . \\ . \\ . \\ . \\ \Delta x_n \end{bmatrix} = \begin{bmatrix} 1 & x_{cam_1} & y_{cam_1} & x_{cam_1}y_{cam_1} & x_{cam_1}^2 & y_{cam_1}^2 & x_{cam_1}^3 & x_{cam_1}^2 y_{cam_1} & x_{cam_1}y_{cam_1}^2 & y_{cam_1}^3 \\ 1 & . & & & & & & & & \\ & . & & & & & & & & \\ & . & & & & & & & & \\ 1 & x_{cam_n} & y_{cam_n} & x_{cam_n}y_{cam_n} & x_{cam_n}^2 & y_{cam_n}^2 & x_{cam_n}^3 & x_{cam_n}^2 y_{cam_n} & x_{cam_n}y_{cam_n}^2 & y_{cam_n}^3 \end{bmatrix} \begin{bmatrix} a_x \\ . \\ . \\ . \\ j_x \end{bmatrix}$$

where ΔX is a column vector containing the error between the two above-mentioned angle measurements. Matrix B contains the polynomial form that will be used. Column vector A contains the coefficients corresponding to polynomial matrix B. Camera coordinates (x_{cam}, y_{cam}) are determined by normalizing the measured angle derived from the target pixel coordinates by the FSM field of view. Normalization is based on the coordinate system defined for the FSM described in the operations manual for the Optotune MR-15-30 [11].

$$x_{cam} = \frac{\tan(\theta_{cam_x})}{\tan(50°)} \tag{4}$$

$$y_{cam} = \frac{\tan(\theta_{cam_y})}{\tan(50°)} \tag{5}$$

Our goal with calibration is to determine coefficient matrix A. The coefficient matrix A was solved by calculating the pseudoinverse of matrix B:

$$A = (B^T B)^{-1} B^T \Delta X \tag{6}$$

Once coefficients have been solved for, corrected FSM pointing coordinates (x_{fsm}, y_{fsm}) can be estimated for any coordinates in the camera field of view as follows:

$$x_{fsm} = x_{cam} - \Delta X(x_{cam}, y_{cam}) \tag{7}$$

$$y_{fsm} = y_{cam} - \Delta Y(x_{cam}, y_{cam}) \tag{8}$$

We evaluated the same data-set using the polynomial fit to correct for errors. Post-calibration error standard deviation for the horizontal and vertical axes was 0.190 and 0.147 degrees, respectively.

2.4 Fixed Target Testing

Testing was performed to verify the ability of the OLTS to reliably detect and hit fixed targets as a key milestone. Preliminary tests were performed with a laser pointer to provide visual confirmation of the system's performance for troubleshooting. It was assumed if the system can reliably hit the target using a laser pointer, so too could a LRF range the target reliably on the same platform. Further, these tests were intended to provide us with experience and insight when designing future testing procedures for the OLTS. Future functional tests to be performed are discussed in section 2.6.

The target used for laboratory testing was a white 3x3x3 inch wooden cube with five Vicon motion capture markers attached. This target was chosen to accommodate the minimum of three motion capture markers required for the Vicon motion capture system and to be of adequate size to be detectable by the optical cueing camera from a distance of 5 m, the size of our laboratory testing area. The target can be seen in Fig. 6.
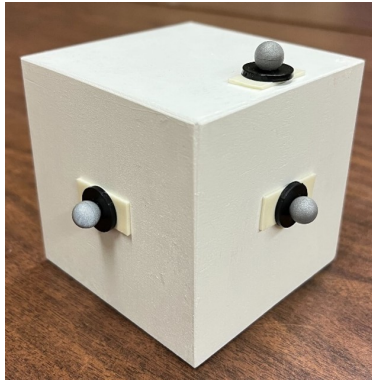
Fig. 6: 3 inch cube target for preliminary tracking tests.

Fixed target tests were determined to be successful if the system fulfills two key criteria. First, the OLTS had to reliably identify fixed targets with the optical cueing camera. Second, the system must consistently hit the center of the detected target at different locations throughout the system field of view without error exceeding 1 degree in both axes. These error bounds represent the system being capable of reliably hitting a target of 17.5 m from a distance of 1 km. These tests were performed without the use of a search pattern.

Procedures for gathering stationary testing data were identical to those used to calibrate the system. The error was determined by comparing a system-determined measurement with a manual truth measurement. We also observed whether the target is hit visually during each system measurement.

Results
Stationary testing was performed with the target at a distance of 2 m from the system. Results from an independent stationary test of twenty locations resulted in a measured mean error of -0.02 degrees for the horizontal axis and -0.28 degrees for the vertical axis. The mean error suggests that the system is biased to aim slightly below the center of detected targets in general. The standard deviation of errors was found to be 0.33 degrees and 0.37 degrees for the horizontal and vertical axes, respectively.

Fig. 7 illustrates that stationary test errors are bounded within 1 degree for both axes. It is also clear that the error calculated for the independent stationary test is more varied than that of the calibration data set. The results of the stationary test will help inform future control aspects of the system, especially when implementing predictive capabilities and setting scanning pattern parameters.
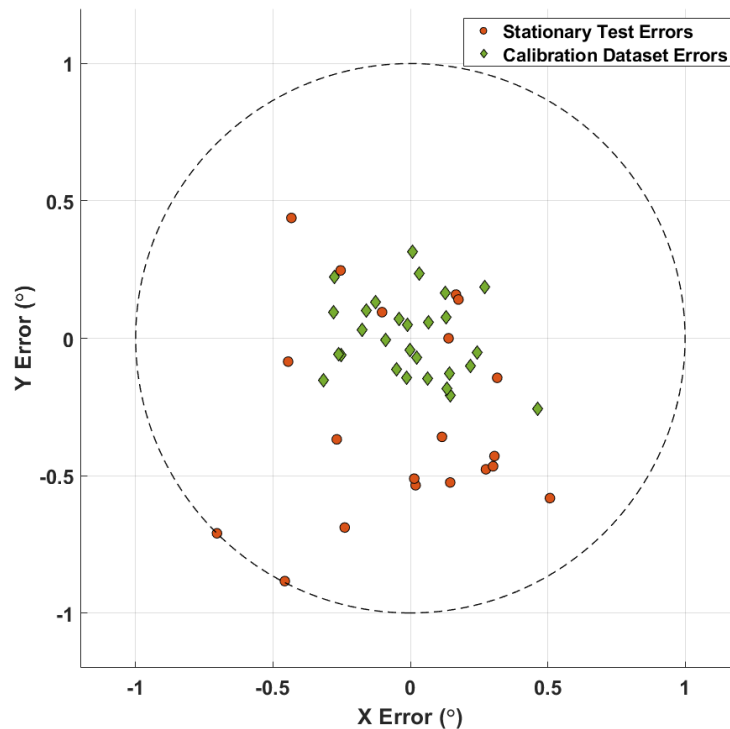
Fig. 7: Summary of fixed target calibration and test errors; one degree bounding circle.

During testing it was noted that the target was not reliably identified by the optical cueing camera. We suspect that lighting conditions and viewing angle heavily affected the performance of the detection algorithm as the system had the most difficulty identifying the target when the target was not normal to the system or when harsh shadows effected one side of the target. Testing of the vision system at distances greater than 2 m yielded drastically lower performance from the vision system, solutions to improving performance of the vision system are discussed briefly in Section 2.6.

2.5 RSO Reflectivity Testing Experimental Apparatus

To determine the OLTS's expected maximum range, we will be experimentally measuring the reflectivity of a number of spacecraft materials using an in-house RSO reflectivity experimental apparatus. This apparatus is a bench-top prototype of a tunable diode laser absorption spectrometer (TDLAS). The design consists of an infrared distributed feedback tunable diode laser (TDL) with an operational wavelength centered at 2700 nm, an infrared HgCdTe photodiode (PD) capable of detecting between 2000 and 10500 nm, and custom control circuitry based on the National Instrument's myRIO-1900 microcontroller.

The TDL is temperature and current controlled, with the temperature held at 35°C, and its supplied current altered to change output wavelength and power. The laser's tunable wavelength range is 2700 ± 2 nm. However this wavelength range is not expected to impact the experimental results. The PD operates at -78°C. Both components are temperature controlled with manufacturer-installed thermo-electric coolers (TECs). The TDLAS is currently operating using a solder board-based circuit, however, an improved printed circuit board is currently being developed. The TDL employs a transconductance amplifier to turn the microcontroller's voltage control signal into a current. The PD employs a transimpedance amplifier to turn the PD's output current signal into a readable voltage signal. The PD operates in photovoltaic mode. Both TECs are controlled with a 100 kHz pulse width modulated signal, bi-directional TEC H-bridge circuit.

Using the RSO reflectivity experimental apparatus, we will measure the reflectivity of five samples that are representative of common spacecraft materials, shown in Fig. 8, as well as a protected silver mirror to provide a high-reflectivity baseline with a reflectivity, R_{avg}, greater than 98% in the 450-10000 nm range.
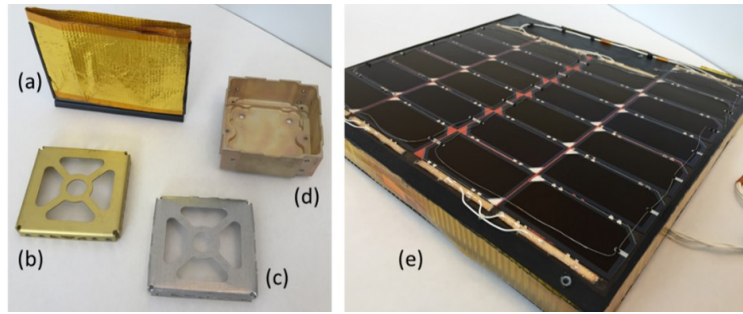
Fig. 8: Sample targets: (a) multi-layer insulation, (b) yellow-anodized aluminum, (c) plain aluminum, (d) alodine aluminum, and (e) multi-material spacecraft test coupon.

To measure reflectivity, the TDL's emitted beam is deflected off the nominal TDL axis/path (the normal defined from the center of the TDL's emitting face) using optical mirrors with $R_{avg} > 98\%$ in the 450-10000 nm range and kinematic mounts. Fig. 9 shows a 3D mock up of the experimental apparatus, the geometry of the beam path, and how the off-axis deflection of the TDL beam will work. Each sample is positioned at a pre-defined distance on the sample mount at the end of the optical breadboard during testing. The mirrors are mounted to a rotation platform, allowing precise angular rotation between the beam and mirror. Care will be taken to ensure that the center point of the mirror is on the axis of rotation.
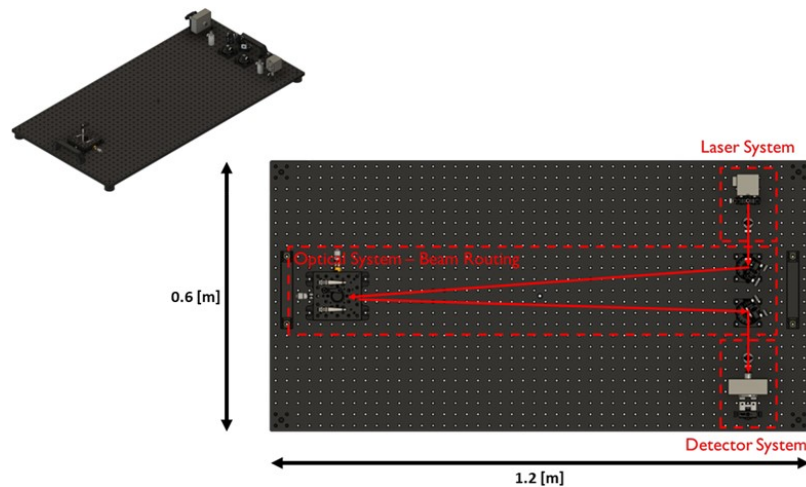

Fig. 9: Top-down and isometric views of the experimental apparatus and ideal beam routing.

The TDL includes an XY adjustable collimation lens, mounted to the face of the laser, to ensure proper laser collimation. Prior to testing, the TDL's beam divergence will be characterized using IR paper at various distances. Additionally, clipping of the laser signal on the receiver due to beam divergence will be minimized during alignment. To ensure no backscattered light damages the TDL while aligning the test apparatus, the laser will be operated at its minimal operation current of 50 mA.

Thermal drift on the TDL and PD might be a significant source of error as both the TDL's output and PD's output are a function of operating temperature. To address this, the PD's TO8 heatsink has been attached to a larger, external heatsink. It has been found that to properly achieve the target operating temperature, the PD's external heatsink must be actively cooled with a DC fan and that care must be taken to ensure that the experimental apparatus is thermally isolated from the ambient environment, while still maintaining ambient temperature. To assist with temperature control, the apparatus will be surrounded by a foam housing and external fans will be used during testing.

Prior to testing, the instrument will be calibrated by sweeping the laser through its entire output range onto a laser power meter, which will be related to output wavelength. This will be repeated with the PD employed to characterize

the PD's power-wavelength-output current. This characterization will be conducted in the same environment and under the same conditions as the experiments to be conducted.

2.6 Discussion and Future Work

Based on the results of the aforementioned tests and the goals of the SPACEDUST program it is evident that there are various aspects of the OLTS that still require work and further testing. Time lag may be addressed by implementing parallel processing of images and mirror pointing, as well as utilizing predictive models for tracking moving targets. It appears that training of the vision system to account for more lighting conditions and farther target distances is also required. The correction of optical distortions should also be implemented to ensure mirror angle data is accurate and reliable when used for analysis.

Further work is required to verify the OLTS's abilities. The fixed target test will have to be re-run after integrating the LRF into the system and making the above mentioned improvements. More controlled slow moving tests will be used to characterize system responsiveness. The system has yet to be flown on the DJI M300, an important requirement for achieving the planned fast target tracking tests outlined earlier. The fast target tests will be an important stress-test on the vision system, FSM, and LRF working in tandem.

Future laboratory tests will include additional functional testing of the optical/laser ranging sensor when detecting slow-moving targets with angular speeds less than 1 deg/s. Material reflectance measurements to determine the optical/laser sensor's maximum expected range are also underway. These material reflectance measurements will use a separate apparatus, based on a 2.7 μm bench-top distributed feedback laser. Future field testing will consist of tracking a fast-moving target, dropped from a helicopter, with the optical/laser ranging sensor mounted on an aerial drone, to emulate the high angular rates that occur during an orbital conjunction event.

2.6.1 Future OLTS Testing

Analytical methods were used to determine the typical angular tracking rates that the system will need to achieve. The simplified scenario of two objects orbiting Earth in the same plane but in opposite directions was examined. We found that for the majority of a one orbit cycle the angular tracking rate did not exceed 0.1 deg/s, but during flyby, the maximum angular rate increased dramatically for a very short period. The system will be tested for typical flyby angular rates during the final fast target tests, expecting a target maximum angular rate exceeding 44 deg/s. An angular rate of 1 deg/s was deemed sufficient to demonstrate the system's ability to track slow-moving space objects.

Testing will be performed to determine the ability of the system to track slow-moving targets with speeds below 1 deg/s. The target consists of the target cube affixed to a metal rod, movement is achieved by having an operator manually move the target in front of the OLTS without obscuring the target. A high accuracy Vicon motion tracking system with an accuracy of 0.1 mm will be utilized to provide objective measurements of the target for comparison with system angular measurements. A figure of the laboratory slow target testing area can be seen in Fig. 10, green tape on the ground denotes the OLTS camera's FOV.

Fig. 10: Slow testing area, the Vicon system provides motion capture coverage throughout the entire OLTS FOV marked by tape.

To evaluate the sensor prototype's performance when detecting objects moving at high angular rates, as will occur during an orbital conjunction event, we will conduct field testing at CFB Gagetown in the fall of 2023. This field test will consist of dropping a streamlined aluminum target from a helicopter at heights between 500 m and 1,000 m. The prototype will detect and track the object while the prototype is mounted on an aerial drone, hovering at 100 m above the ground at a 90 m horizontal distance from the drop point. Based on previous field tests, we expect the target's velocity to exceed 70 m/s and the relative angular rate, as perceived by the prototype, to exceed 44 deg/s.

To detect the fast-moving target, the network is being re-trained using the same YOLOv5s network on a set of scaled analogues of the fast-moving target. These analogues consist of a set of 6 mm diameter aluminum cylinders, imaged on various sky backgrounds.

2.6.2 Bench-Top Reflectivity Tests

The test objectives for the reflectivity experiments are to collect measurement data for each sample target and analyze their reflectivity relative to other samples under various test conditions. Success will be characterized by successful experimental operation and data collection, and meaningful representation and discussion of said data. The aim is to determine the current apparatus' capabilities and limitations for range-determination of reflectivity experiments, and to see the effects various materials have on laser reflectivity.

Analysis will be provided for short-range specular reflection under various laser operational conditions, short range diffuse reflection, and long-range specular reflection. For these experiments, the signal-to-noise ratio will be roughly calculated via comparison of experimental signals to a dark measurement (system noise), an ambient measurement (ambient noise), and a long laser exposure measurement (to help determine potential laser and/or detector instability). Confidence is higher for short-range and simplistic DC signals, so the following test plans are defined accordingly.

The first and second set of tests will investigate short-range specular reflectivity and the repeatability of the apparatus. For these tests the high-reflectivity target will be used as a baseline to normalize measurements. Each of the spacecraft sample targets will be measured once, and the high-reflectivity optical mirror will be measured three times as the first and last measurements. The data acquisition period will be set to 60 seconds at 1000 Hz acquisition rate, a simple DC input waveform will be applied, and off-axis distance will be set to a fixed value within the 0.25-0.50 m range. The orientation of the samples will be adjusted to measure specular reflection. The second set of tests (after the first run-through of samples) will investigate repeatability by simply repeating the first set of tests. These results are intended to provide confidence in results and reduce the impact of human error.

The third set of tests will investigate the effects of a non-DC waveform on the reflected signal (e.g., a low-frequency ramp or sinusoidal signal). This test is done to offset any potential thermal drifting in the detector since a periodic increase/decrease in signal will be easily distinguished from the background and potential signal drift. For these tests, a subset of samples will be selected (the optical mirror and two spacecraft samples). A well-known non-DC waveform will be applied while the remaining conditions will be set according to the first set of tests. The high-reflectivity target will again be used as a baseline to normalize measurements.

The fourth set of tests will investigate diffuse reflection. For these tests, a subset of samples will be selected (two spacecraft samples that are likely to have significant diffuse components). The orientation of the mirror-receiver off-axis beam routing mirror will be adjusted to measure diffuse reflection (e.g., offsets of approximately 10, 20, 30 degrees) while the remaining conditions will be set according to the first set of tests. This ensures that the angle of incidence of the incident beam on the sample remains the same and allows for comparison between the specular tests. Test Set 4 will be conducted immediately after Set 1, 2, and 3 for the selected samples, to ensure that the angle of incidence between the laser beam and sample remain the same. The mirror-receiver angle will be altered between a range of 0-30 degrees, in stepwise increments of 5 degrees.

The fifth set of tests will investigate the effect of off-axis distance. For these tests, a subset of samples will be selected (optical mirror and two spacecraft samples). The distance will be adjusted to the maximum range allowed by the test environment while the remaining conditions will be set according to the first set of tests. If the test environment allows, the test will be conducted at various increasing off-axis distances. It is expected that the multi-layer insulation and multi-material spacecraft test coupon will have significant diffuse reflections, and weak specular reflections. This is due to their material properties and specific surface finishes (rough). It is unclear how the surface finish on the remaining samples will affect specular/diffuse reflections, but based on preliminary visual inspection, it is expected

that the specific beam target location may have significant impact on reflections, as there are scratches and numerous imperfections.

3. SAR RSO RANGING

In this section, we first describe our methodology for extracting RSO data from SAR data. Using this methodology, we extracted RSO data from both simulation results and real SAR imagery, the results of which are discussed. The section ends by providing our preliminary conclusions, and discussing future work.

3.1 Methodology

When a SAR instrument transmits signals to the ground for Earth remote sensing, the reflected signal contains returns from both ground targets and any RSOs between the SAR antenna and the target. Fig. 11 depicts the format of the received data, where each range line is drawn below the previous one, to form a two-dimensional array of data. The received range line could contain the RSO echoes, the ground target echo, or a combination of echoes from the RSO and ground target. In Fig. 11, it is assumed that the relative velocity between RSO and the SAR sensor is small enough that the RSO is located within the SAR field of view (FOV) during the SAR illuminating period. If the relative velocity between RSO and SAR is large, the echo from the RSO could appear in the SAR FOV over a significantly short duration, and be received in only a single range line or several range lines. Since the relative velocities are different, the RSO target can be detected through the analysis of the Doppler spectrum of range lines.
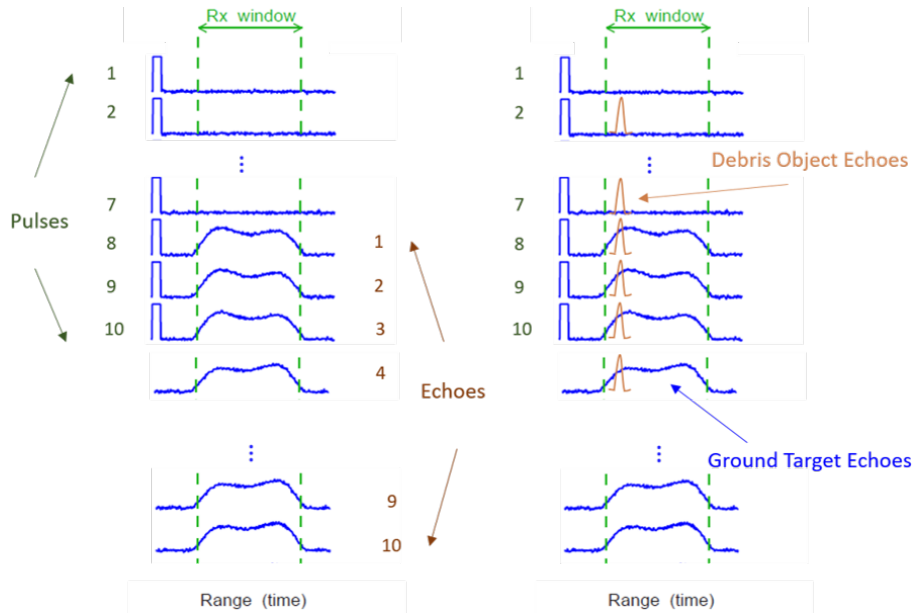

Fig. 11: Illustration of the format of normal data reception in a hypothetical computer signal memory for ground target (Left) and RSO and ground target (Right).

Usually, after receiving the reflected signal, SAR signal processing algorithms are used to form a SAR image focused on the ground target signal, filtering out any received RSO signals. Similarly, a bank of matched filters can be used to search and detect RSO signals within raw, unprocessed SAR data. Assuming that the SAR is illuminating a point RSO target with a series of chirp signals, the received raw data after demodulation can be described by [12, 13].

$$s_0(\tau, \eta) = A_0 \omega_a(\eta - \eta_c) \exp\left(-j\frac{4\pi R(\eta)}{\lambda}\right) \text{rect}\left[\frac{\tau - \frac{2R(\eta)}{c}}{T_p}\right] \exp(j\pi K_r(\tau - \frac{2R(\eta)}{c})^2) \tag{9}$$

where A_0 is signal amplitude, which depends on the strength of the transmitted signal, target reflectivity, and other factors; ω_a is the antenna gain (azimuth envelope), which can be approximated as a sinc-squared function; τ is the fast

time (range time); η is the slow time (azimuth time); η_c is the beam center offset time; $R(\eta)$ is the instantaneous slant range; λ is the signal wavelength; T_p is the chirp duration; K_r is the chirp modulation frequency rate; c is the speed of light; and $j = \sqrt{-1}$. rect[·] and exp(·) represent the rectangular function and the exponential function. The Range Doppler Algorithm (RDA) could be used to process SAR raw data with a matched filter to detect a RSO target. An RDA functional block diagram is shown in Fig. 12.
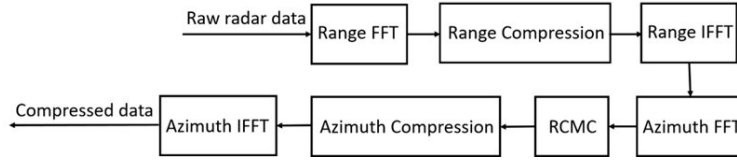

Fig. 12: Functional block diagram of RDA.

After being processed by the RDA, the compressed data can be expressed as [12].

$$s_{ac}(\tau, \eta) = A_0 p_r(\tau - 2R_0/c) p_a(\eta) \exp\left(-j\frac{4\pi R_0}{\lambda}\right) \exp(j2\pi f_{\eta_c}\eta) \tag{10}$$

where R_0 is the slant range of closest approach, and $f(\eta_c)$ is the Fourier transform of η_c. p_a and p_r represent the pulse envelope, a sinc-like function.

3.2 Simulation Results

Based on a theoretical RSO reflected signal model, simulations were made to examine the viability of SAR imaging for RSO detection and ranging. Table 1 shows the simulation parameters, where values were chosen based on representative spaceborne SAR parameters [12]. Fig. 13 compares the Doppler spectrum for ground targets only and a combination of ground targets and RSOs. There is an obvious peak in the right plot of Fig. 17, which was caused by the RSO's relative velocity with respect to the satellite. It can be concluded that the Doppler information can be beneficial for differentiating the RSO from the ground target to detect fainter RSO signals.

Table 1: Simulation Parameters of Spaceborne SAR.

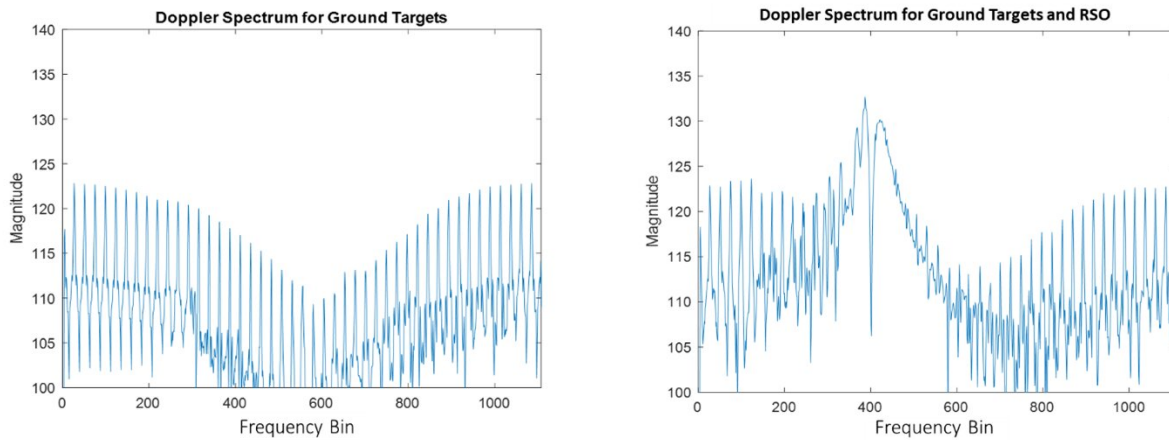| Parameter	Value
Carrier frequency	5.3 GHz
Chirp pulse duration	40 μs
Chirp bandwidth	20 MHz
Range sampling rate	24 MHz
Slant range swath width	50 km
Antenna length	10 m
Synthetic aperture length	4.8 km
Pulse repetition frequency (PRF)	1635 Hz

Fig. 13: (Left) Doppler spectrum for ground targets; (Right) Doppler spectrum for ground targets and RSO.

In this work, the echoes from ground targets are treated as clutter/noise when extracting an RSO echo from SAR data. In this case, the travelling distance and reflectivity of the target are vital to evaluate if the RSO signal is obscured by ground target signal. In this work, it is assumed that the amplitude of the RSO target signal is not contaminated by the ground targets because the travelling distance of the RSO could be much smaller than the ground targets. The reflectivity of the target depends on the target's material properties, the target size, target shape, operating frequency, amongst other factors. Fig. 14 shows the RSO range data extraction with different effects of target radial velocity and azimuth velocity on the SAR image. The radial velocity component produces an azimuth displacement of the target due to a Doppler offset, while the azimuth velocity component produces a Doppler slope change causing a defocusing in the moving target image [14, 15].
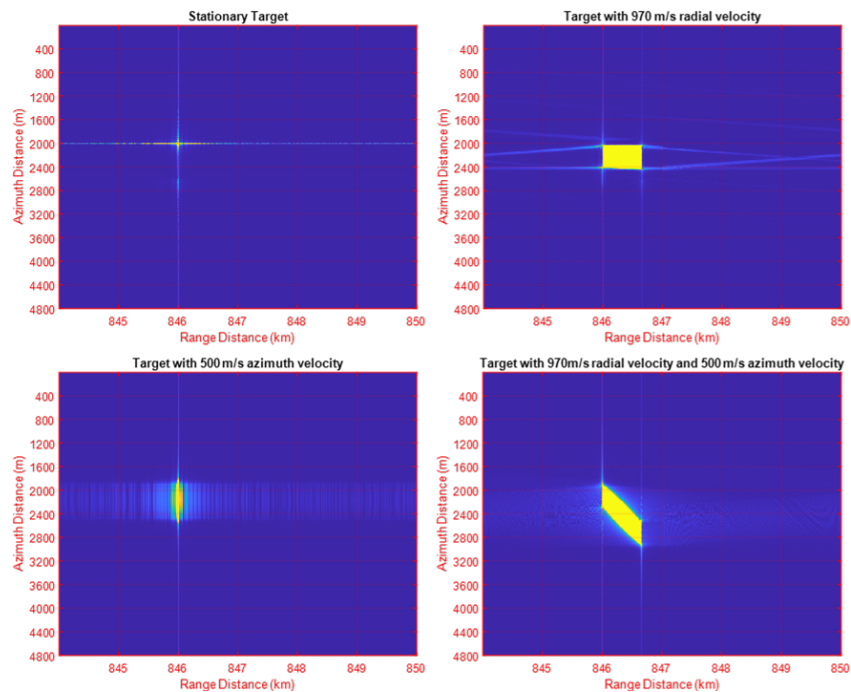

Fig. 14: RSO ranging data extraction with different radial and azimuth velocity.

3.3 Real SAR Imagery Results

Since Sentinel-1 raw data is publicly available, it was used in this work to examine the feasibility of using SAR images to detect RSOs, using the ISS as a target. Ansys STK [16] was first used to search for opportunities in which Sentinel-1 may have imaged the RADARSAT Constellation Mission (RCM) and the ISS. Since the Sentinel-1 sensing time is not continuous, code was written to check the availability of Sentinel-1 imagery during the STK opportunity time list. There was no Sentinel-1 imagery found for RCM during the opportunity time list, however, 16 Sentinel-1 image sets with predicted ISS detections were found from January 1st 2022 to July 12th 2023.

After further studying these 16 Sentinel-1 image sets, only one image set contained an ISS target signal. This discrepancy between predicted and actual ISS signal-containing imagery was caused by the slant range R_{slant} between the ISS and Sentinel-1, which must satisfy certain conditions to ensure that the echo reflected from the target is recorded by the receiver. These conditions can be expressed as

$$\frac{[(SWST - \text{pulse length} + N \times PRI] \times c}{2} \leq R_{\text{slant}} \leq \frac{[SWL + N \times PRI] \times c}{2} \tag{11}$$

where the sampling window start time ($SWST$) and the sampling window length (SWL) are defined in Fig. 15. PRI is the pulse repetition interval, and N is an integer.
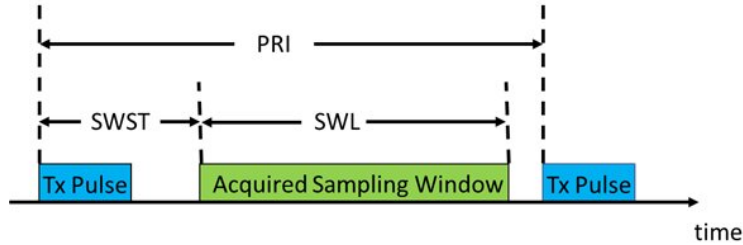

Fig. 15: Definition of SWST and SWL.

Sentinel-1 operated with Interferometric Wide (IW) swath mode for all these 16 Sentinel-1 imageries. IW mode data is acquired in three sub-swaths with different incidence angles, elevation angles, PRIs, etc. In this case, the target could be missed by scanning between different sub-swaths. For example, if Sentinel-1 is operating with IW3 swath mode, and the target is located in the IW1 FOV, the target will not be detected. Based on these findings, it could be found that there are few opportunities for Sentinel-1 raw data to contain ISS target reflections. However, if a large number of SAR satellites were used to detect RSO targets, their combined capabilities could significantly increase the probability of detecting RSOs using SAR imagery.

For the Sentinel-1 imagery containing an ISS reflection signal, the STK results are shown in Table 2. The ISS is moving away from the Sentinel-1 satellite with a relative radial velocity of 2.64 km/s, which is expected to bring in a Doppler shift at -0.095 MHz. The transit time is 0.641 s, during which the slant range and relative velocity are almost constant. In this case, a coherent integration is conducted on all pulse responses with ISS target echoes to remove the noise effect and increase the signal to noise ratio (SNR). The Doppler spectra with single range line is shown in Fig. 16 and with all range lines is shown in Fig. 17. A set of same length data, which is located adjacent to the ISS transit period, was extracted and used for comparison in Fig. 16 and Fig. 17.

Table 2: STK results for Sentinel-1a imaging ISS.

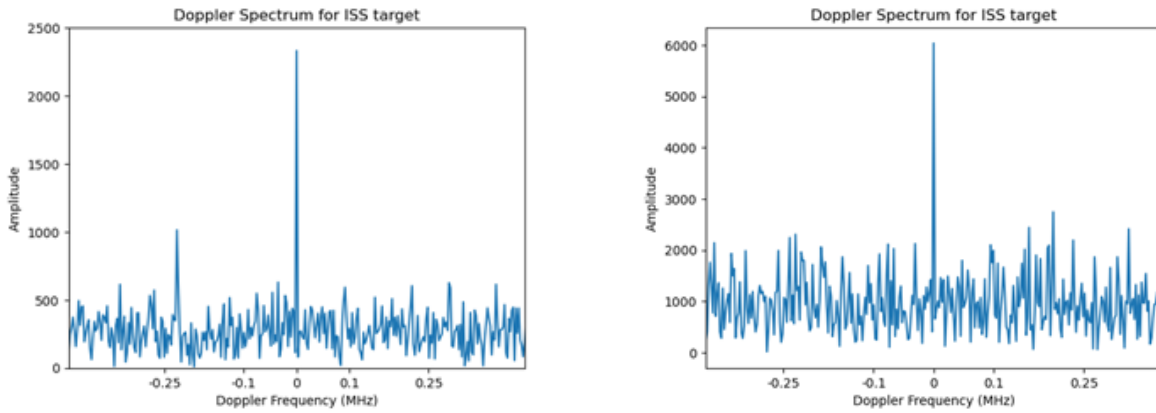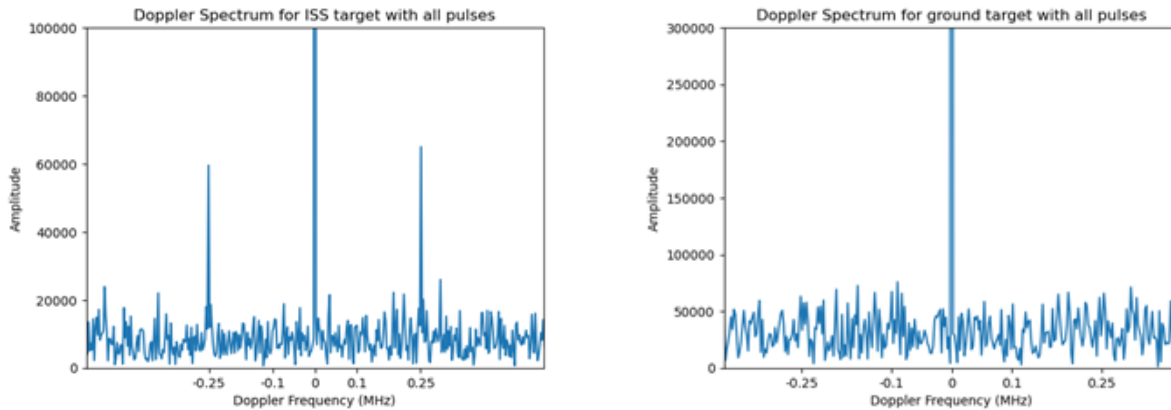| Parameters	Values
Start time	28:49.5 min:s
Stop time	28:50.1 min:s
Duration	0.641 s
Pulse length	52.4 μs
Pulse repetition interval (PRI)	582.37 μs
SWST	88.61 μs
SWL	371.98 μs
Slant range	315.21 km
Relative radial velocity	2.64 km/s

Fig. 16: Doppler spectrum with single range line ISS pulse response.

(a) ISS target.

(b) Ground target.

Fig. 17: Doppler spectrum with all ISS pulse responses.

Fig. 16 gives an example of a single range line Doppler spectrum, in which a peak appears at -0.25 MHz. However, this is not consistent for every range line during the ISS's transit time. A coherent sum result of all pulses is shown in Fig. 17a. There are two obvious peaks at ± 0.25 MHz, while, the ISS peak is expected to be located at -0.1 MHz. Compared to the ground target (Fig. 17b), there is no obvious peak in the Doppler spectrum. The SAR figure after the matched filter was also checked, but has no obvious target signature was discerned. From the STK results, the slant

range between the ISS and Sentinel-1 is around 315 km. However, from the Sentinel-1 data, the correlation result shows that the target slant range could be 272 km or 359 km because the extracted range has a PRI time travelling time ambiguity.

The meaning for these peaks is still under investigation and requires verification. There are some key areas to be investigated: whether there are other RSOs around Sentinel-1 during this period; and if the complex structure of the ISS and if relative rotation motion will give a different Doppler frequency.

3.4 Discussion and Future Work

Based on the results in Section 3.3, it can be concluded that existing SAR imaging is viable for RSO detection and ranging. However, there are many constraints for this application:

- Limitations in RSO range. The receiver is not always turned on, and there is a limited window to receive the reflected signal. For example, if the RSO is too close to the satellite, the reflected signal cannot be received because it falls out of the SAR's received signal window.

- Limitations in RSO size. Small RSOs, in the cm size range and smaller, have smaller radar cross sections, which can be masked by the ground target echoes.

- Limitations in RSO velocity. If the relative velocity in the satellite looking direction is too large and generates a Doppler frequency greater than $PRF/2$, there is a Doppler aliasing problem.

- Limitations in detectable region. SAR beams are narrow and looking down to the Earth, which only illuminates a small cone in space. This limits the probability of RSO detections by SAR because of the limited FOV.

- Limitations in SAR operations. SAR platforms do not operate continuously, and some acquisition modes scan over the Earth, which greatly reduces the opportunities for illuminating RSOs in the SAR FOV.

- Algorithms applied to existing SAR images are expected to perform better on RSOs with known locations and speeds. Otherwise, there will be some uncertainty in determining if there is a RSO or not, especially for fast moving and small RSOs.

For RSO extraction, it is recommended that raw SAR data be obtained and used, in order to better search for RSO in each range line. A rough estimation of RSO range and speed can be conducted before processing the SAR image, which will greatly reduce the amount of computation time spent searching for appropriate range and azimuth matched filters. Through iterative SAR analysis, the RSO range and speed can be refined. Furthermore, the relative velocity of the RSO will produce a peak in the Doppler spectrum, which can be used to extract RSO information for fainter detections.

In this work, only the case of Sentinel-1 sensing ISS was investigated. Future work will focus on enlarging the RSO and SAR imagery datasets. Expanding the RSO catalogue used in our analysis would allow us to discern the source and path of returned signals during ISS transits through the SAR sensor's FOV. Additionally, the RSO target was assumed to be a point target in the simulation, which may not be a good assumption in the real SAR signals. The complex structure of large RSOs and relative their rotation motions will result in different Doppler spectra and SAR images, which is worth studying in the future.

4. CONCLUSIONS

The development of space situational awareness systems and techniques is an important area for the continued success and safety of space-based missions. In this paper we have presented the preliminary work for the development of two such technologies complemented by discussion of future work for each. Additionally, we have presented the preliminary design for a optical/laser RSO detection prototype as well as a method for detecting RSOs in existing SAR imagery. The optical/laser ranging system uses a combination of a computer vision-enabled cueing camera and a steerable laser rangefinder to provide users with relative RSO angle and range data that can be used to reconstruct the object's orbit. A platform to explore the effects of RSO reflectivity on optical time-of-flight ranging methods is being developed. The SAR-based RSO detection method is capable of extracting RSO detections from existing SAR imagery captured by Earth observation SAR platforms.

While the results for these methods are preliminary, they suggest that both RSO detection methods are feasible but merit further investigation, development, and evaluation. We believe that the development and evaluation of both optical/laser detection and SAR imagery systems will be key components of future space situational awareness missions. Sensors and methods such as those described in this paper are a necessity for space domain awareness and are an important step in ensuring our continued use of space for generations.

5. ACKNOWLEDGEMENTS

REFERENCES

[1] Michael A. Steindorfer, Georg Kirchner, Franz Koidl, Peiyuan Wang, Beatriz Jilete, and Tim Flohrer. Daylight space debris laser ranging. *Nature Communications*, 11(1), 2020.

[2] Yagiz Kaymak, Roberto Rojas-Cessa, Jianghua Feng, Nirwan Ansari, MengChu Zhou, and Tairan Zhang. A survey on acquisition, tracking, and pointing mechanisms for mobile free-space optical communications. *IEEE Communications Surveys Tutorials*, 20(2):1104–1123, 2018.

[3] Matthew Driedger, Aref Asgari, and Philip Ferguson. Feasibility of gathering resident space object range measurements using in-orbit observers. *IEEE Journal of Radio Frequency Identification*, 6:250–257, 2022.

[4] Alexandre Pollini, Christophe Pache, and Jacques Haesler. CSEM space lidars for imaging and rangefinding. In *IGARSS 2018 - 2018 IEEE International Geoscience and Remote Sensing Symposium*, pages 1849–1852, 2018.

[5] JENOPTIK Optical Systems. `https://www.jenoptik.us/-/media/websitedocuments/optics/sensor/dlem_datasheet_20230818.pdf`.

[6] Terrasar-x image of the month: The international space station (ISS). `https://www.dlr.de/en/latest/news/2010/20100304_terrasar-x-image-of-the-month-the-international-space-station-iss-_22539/@@download/file`.

[7] Siddharth Dave, Ryan Clark, Gabriel Chianelli, and Regina Lee. *Machine learning implementation for in-orbit RSO orbit estimation using star tracker*. Advanced Maui Optical and Space Surveillance Technologies Conference (AMOS), 2020.

[8] Glenn Jocher, Ayush Chaurasia, Alex Stoken, Jirka Borovec, NanoCode012, Yonghye Kwon, Kalen Michael, TaoXie, Jiacong Fang, imyhxy, Lorna, (Zeng Yifu), Colin Wong, Abhiram V, Diego Montes, Zhiqiang Wang, Cristi Fati, Jebastin Nadar, Laughing, UnglvKitDe, Victor Sonck, tkianai, yxNONG, Piotr Skalski, Adam Hogan, Dhruv Nair, Max Strobel, and Mrinal Jain. ultralytics/yolov5: v7.0 - YOLOv5 SOTA realtime instance segmentation. `https://doi.org/10.5281/zenodo.7347926`, November 2022.

[9] Optotune MR-15-30: Dual axis fast steering mirror with position feedback. `https://www.optotune.com/mr1530`.

[10] DJI upward gimbal connector for matrice 300 RTK - photo video. `https://www.bhphotovideo.com/c/product/1565974-REG/dji_cp_en_00000266_01_matrice_300_series_upward.html`.

[11] Optotune. MR-E-2 development kit operation manual. `https://www.optotune.com/s/Optotune-MR-E-2-Development-Kit-operation-manual.pdf`, 2019.

[12] Ian G. Cumming and Frank Hay-chee Wong. *Digital processing of Synthetic Aperture Radar Data: Algorithms and Implementation*, page 108–110. Artech House, 2005.

[13] Weijie Xia, Yuanyuan Qi, Linlin Huang, and Xue Jin. Missile-borne SAR raw signal simulation for maneuvering target. *International Journal of Antennas and Propagation*, 2016:1–12, 06 2016.

[14] A. Budillon, Vito Pascazio, and Gilda Schirinzi. Multichannel along-track interferometric sar systems: Moving targets detection and velocity estimation. *International Journal of Navigation and Observation*, 2008, 01 2008.

[15] Alessandra Budillon, Christoph H. Gierull, Vito Pascazio, and Gilda Schirinzi. Along-track interferometric sar systems for ground-moving target indication: Achievements, potentials, and outlook. *IEEE Geoscience and Remote Sensing Magazine*, 8(2):46–63, 2020.

[16] Ansys STK — digital mission engineering software. `https://www.ansys.com/products/missions/ansys-stk`.